Article

https://doi.org/10.1038/s41567-023-02266-2

Valley-polarized excitonic Mott insulator in WS_2/WSe_2 moiré superlattice

Received: 8 December 2022

Accepted: 22 September 2023

Published online: 6 November 2023

Check for updates

Zhen Lian[1,10], Yuze Meng[1,10], Lei Ma[1,10], Indrajit Maity[2,10], Li Yan[1], Qiran Wu[3], Xiong Huang[3,4], Dongxue Chen[1], Xiaotong Chen[1], Xinyue Chen[1], Mark Blei[5], Takashi Taniguchi[6], Kenji Watanabe[7], Sefaattin Tongay[5], Johannes Lischner[2], Yong-Tao Cui[3] & Su-Fei Shi[1,8,9]

The strongly enhanced electron–electron interactions in semiconducting moiré superlattices formed by transition metal dichalcogenide heterobilayers have led to a plethora of intriguing fermionic correlated states. Meanwhile, interlayer excitons in a type II aligned heterobilayer moiré superlattice, with electrons and holes separated in different layers, inherit this enhanced interaction and suggest that tunable correlated bosonic quasiparticles with a valley degree of freedom could be realized. Here we determine the spatial extent of interlayer excitons and the band hierarchy of correlated states that arises from the strong repulsion between interlayer excitons and correlated electrons in a WS_2/WSe_2 moiré superlattice. We also find evidence that an excitonic Mott insulator state emerges when one interlayer exciton occupies one moiré cell. Furthermore, the valley polarization of the excitonic Mott insulator state is enhanced by nearly one order of magnitude. Our study demonstrates that the WS_2/WSe_2 moiré superlattice is a promising platform for engineering and exploring new correlated states of fermion, bosons and a mixture of both.

Semiconducting moiré superlattices of transition metal dichalcogenide (TMDC) monolayers, especially those formed by the WS_2/WSe_2 heterobilayer, have been shown to exhibit strong electron correlation owing to the formation of flat moiré miniband and strong Coulomb interaction[1–7]. In two-dimensional systems, in general, the Coulomb interaction is enhanced because of reduced dielectric screening. In a TMDC moiré superlattice, the considerably larger effective mass of flat moiré miniband[8] further reduces the kinetic energy compared with that in TMDC monolayers. As a result, the degree of electron–electron interaction is strongly enhanced. Exciting electronic correlated states with high transition temperatures have been demonstrated and investigated. In particular, the strong electron interaction can result in the spatial ordering of charge carriers in the moiré superlattice, forming Mott insulator and generalized Wigner crystal states[1–4,9,10]. Meanwhile, the strong Coulomb interaction in TMDC semiconductors also leads to strongly bound electron–hole pairs, that is, robust excitons with valley degree of freedom[11–13]. It is thus intriguing to investigate whether these optically excited excitons would form strongly correlated bosonic states[14,15] in a TMDC moiré superlattice owing to reduced kinetic energy, which will allow the exploration

[1]Department of Chemical and Biological Engineering, Rensselaer Polytechnic Institute, Troy, NY, USA. [2]Department of Materials and the Thomas Young Centre for Theory and Simulation of Materials, Imperial College London, London, UK. [3]Department of Physics and Astronomy, University of California, Riverside, CA, USA. [4]Department of Materials Science and Engineering, University of California, Riverside, CA, USA. [5]Materials Science and Engineering Program, School for Engineering of Matter, Transport and Energy, Arizona State University, Tempe, AZ, USA. [6]International Center for Materials Nanoarchitectonics, National Institute for Materials Science, Tsukuba, Japan. [7]Research Center for Functional Materials, National Institute for Materials Science, Tsukuba, Japan. [8]Department of Electrical, Computer and Systems Engineering, Rensselaer Polytechnic Institute, Troy, NY, USA. [9]Department of Physics, Carnegie Mellon University, Pittsburgh, PA, USA. [10]These authors contributed equally: Zhen Lian, Yuze Meng, Lei Ma, Indrajit Maity. e-mail: yongtao.cui@ucr.edu; sufeis@andrew.cmu.edu

https://doi.org/10.1038/s41567-023-02266-2

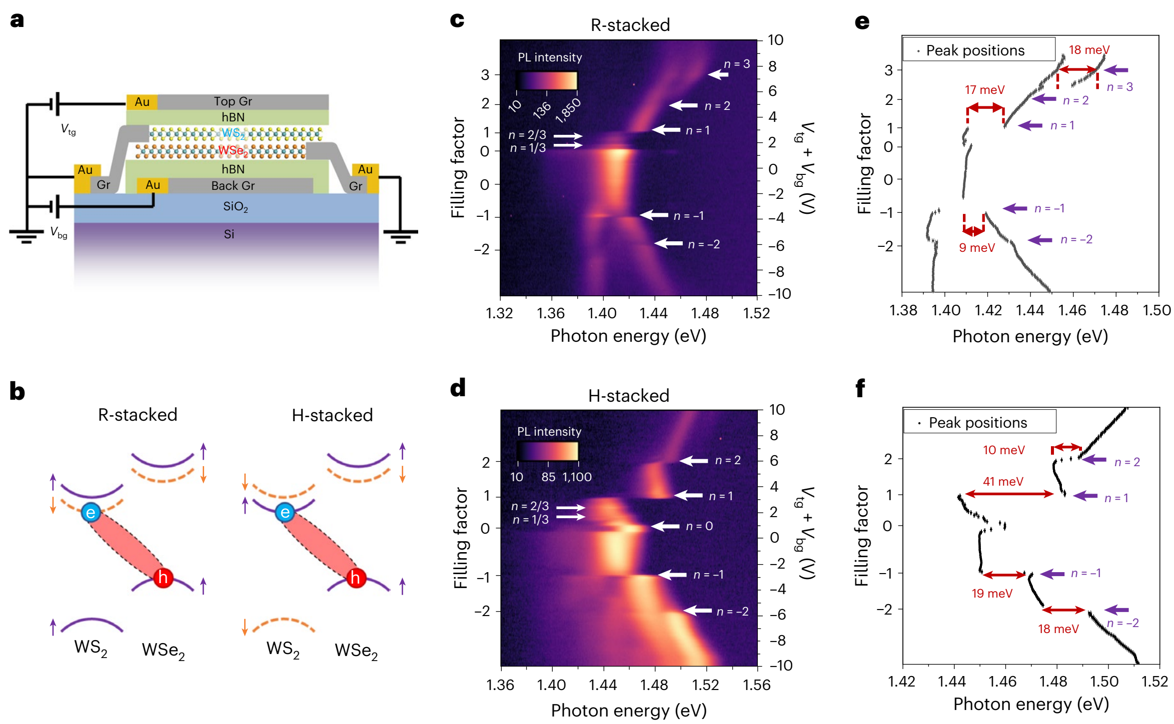

Fig. 1 | Doping-dependent PL spectra of IXs in WS_2/WSe_2 moiré superlattice. **a**, Schematic of the WS_2/WSe_2 device. V_{tg} and V_{bg} denote the top gate voltage and the back gate voltage, respectively. Gr and hBN indicate few-layer graphene flakes and hexagonal boron nitride flakes, respectively. **b**, Schematic of the type II alignment for both R-stacked and H-stacked configurations. **c**,**d**, Doping-dependent PL spectra of the R-stacked (**c**) and H-stacked (**d**) device. **e**,**f**, PL peaks extracted from **c** and **d**, respectively, by fitting the PL spectra with Lorentzian peaks. The region between the two zeros of the filling factor in **c** and **e** indicates the charge-neutral region of the device. The error bars indicate the standard errors extracted from the fitting. The PL spectra were taken with a CW laser excitation centred at 1.96 eV. The excitation power is 5 μW in **c** and 25 μW in **d**, corresponding to an average exciton density around 2.9×10^{11} cm^{-2} and 1.45×10^{12} cm^{-2}, respectively. All spectra were taken at a temperature of 4.2 K.

of bosonic correlated physics in a highly tunable two-dimensional condensed-matter system.

In this paper, we turn to the archetypal WS_2/WSe_2 moiré superlattice whose type II band alignment enables interlayer excitons (IXs)[16,17], with holes residing in the WSe_2 layer and electrons in the WS_2 layer. The permanent dipole moment stemming from the charge separation gives rise to strong repulsion between IXs, rendering this system a promising candidate for realizing the excitonic Mott insulator, a strongly correlated state described by the bosonic Hubbard model[18]. We first use photoluminescence (PL) spectroscopy to show the strong repulsion between electrons and IX at correlated insulating states, which we combine with first-principles calculations to reveal the more extended nature of the IX in the H-stacked (60° twisted) WS_2/WSe_2 moiré superlattice than the R-stacked (0° twisted) configuration. We further show that adding excitons to a charge-neutral moiré superlattice with a density high enough to excite double IX occupation in one moiré unit cell will result in additional high-energy PL emissions owing to IX–IX repulsion, which is about 44 meV for the R-stacking and about 32 meV for the H-stacking. Interestingly, the valley polarization of the IX is strongly enhanced by nearly one order of magnitude when the excitonic Mott insulator state emerges, inspiring future exploration of valley physics in this strongly correlated bosonic system.

We construct angle-aligned WS_2/WSe_2 moiré bilayers using the same dry pick-up method as described in our previous studies[3,19–21] and fabricate devices with dual-gate geometry as schematically shown in Fig. 1a. The application of top and back gate voltages allows us to control the doping and electric field independently. The doping-dependent PL spectra for both R-stacked and H-stacked moiré bilayers can be found in Fig. 1c,d (devices R1 and H1, respectively). The enhanced PL intensity at characteristic carrier densities marks the formation of correlated insulating states at filling factors $n = 1, 2, 3$, that is, one, two or three electrons per moiré unit cell, and also on the hole side at $n = -1$ and -2. Correlated states at fractional fillings of $n = 1/3, 2/3$ are also visible, corresponding to the generalized Wigner crystal states studied previously[1,3]. The zoom-in PL spectra showing fractional filling more clearly for the devices shown in Fig. 1c,d are shown in Extended Data Fig. 1. The PL spectra of another H-stacked device (H5) showing more fractional fillings can be found in Extended Data Fig. 2.

The most pronounced features in Fig. 1c,d are the abrupt blueshifts of IX resonance energy (PL peak) at Mott insulating states of $n = -1$ and 1. The blueshift for the R-stacked device (R1) is around 17 meV and around 9 meV for $n = 1$ and -1, whereas the blueshift for the H-stacked device (H1) is around 41 meV and around 19 meV for $n = 1$ and -1, respectively. We first note that the magnitude of the blueshift at $n = \pm1$ is smaller for the R-stacking than for the H-stacking. Second, the blueshift at $n = -1$ is smaller than that at $n = 1$ in both stackings.

The blueshifts of IX PL at Mott insulating states $n = \pm1$ originate from the electron–exciton repulsion. For example, at the Mott insulator state at $n = 1$ in which each moiré unit cell is occupied by one electron, adding an IX to any moiré unit cell requires an additional energy cost on the scale of the Mott gap (U_{e-e}) owing to the close proximity of the correlated electron and the constituent electron of the IX in the same WS_2 layer. This energy cost will be offset by the Coulomb attraction between the correlated electron in the WS_2 layer and the constituent hole of the IX in the WSe_2 layer (V_{e-h}), which is smaller than U_{e-e} owing to layer separation. This interpretation of the blueshift, combined with theoretical insights gained from first-principles calculations, can explain the two major observations described previously.

The first-principles calculations of band structures for both R-stacked and H-stacked WS_2/WSe_2 moiré heterobilayers are shown

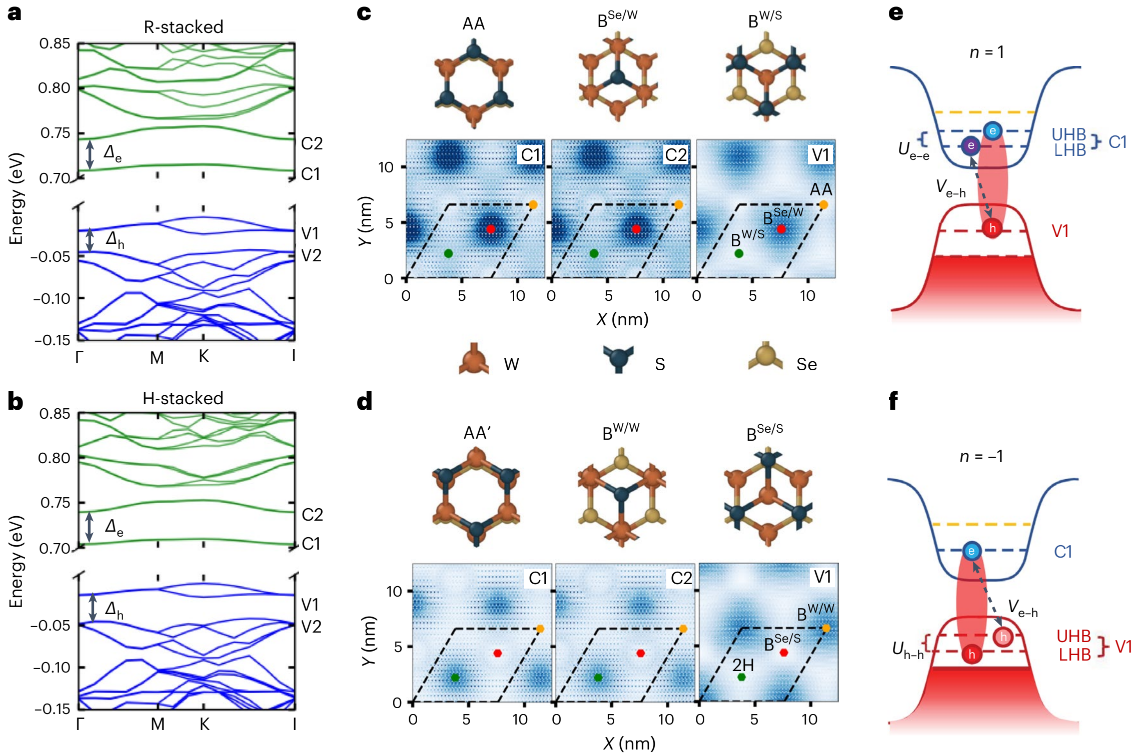

Fig. 2 | Band structure of the WS_2/WSe_2 moiré superlattice. a,**b**, First-principles calculations of the band structure of R-stacked (**a**) and H-stacked (**b**) WS_2/WSe_2 moiré superlattice. **c**,**d**, Bottom: the electron wave function distribution of two conduction bands (C1 and C2) and one valence band (V1) in the moiré unit cell for R-stacked (**c**) and H-stacked (**d**) configurations. The unit cell is marked with dashed lines and the high-symmetry stackings associated with the moiré are marked with circles. Top: the atomic structure of the associated high-symmetry stackings. **e**,**f**, Schematics of adding one IX to the correlated insulating state at filling $n = 1$ (**e**) and $n = -1$ (**f**).

in Fig. 2a,b, respectively. For both R-stackings and H-stackings, there is one flat valence band (V1) isolated from other valence bands with an energy separation Δ_h. There are also two flat conduction bands (C1 and C2) with an energy separation, Δ_e, between them. At K and K′ valleys, the spin is polarized in the valence band, whereas C1 and C2 possess different spins. The values of Δ_h for R-stackings and H-stackings are different, 26 meV and 35 meV, respectively. By contrast, Δ_e is very similar for both R-stackings and H-stackings, 31 and 32 meV, respectively.

It is evident that R-stackings and H-stackings differ strikingly in the electronic wavefunction distribution for each of the flat bands (Fig. 2c,d). In either R-stacked or H-stacked configuration, there are three high-symmetry points that preserve the three-fold rotational symmetry (insets of Fig. 2c,d), which we label with their local stacking configurations. The moiré potential landscape varies at different moiré sites. In the R-stacking, the holes from V1 and electrons from both C1 and C2 are all localized in the $B^{Se/W}$ site. By contrast, in the H-stacking, the holes from V1 are localized in the $B^{W/W}$ site, and the electrons from C1 and C2 are localized at the AA′ site (2H). As the IX ground state consists of an electron from C1 and a hole from V1, the IX will have the electron and hole at the same moiré site in the R-stacking but at different moiré sites in the H-stacking. As a result, the IX will be more extended in the H-stacking, consistent with the shallower moiré potential confinement of excitons in the H-stacking from our calculation (details in Supplementary Section 8) as well as from a recent report[22]. The extended nature of IX in the H-stacking is also consistent with our experimental observations in Fig. 1e,f: in the H-stacked device, the IX PL peak redshifts as soon as electrons or holes are electrostatically introduced, probably owing to the sensitivity of the extended IX to the dielectric screening; by contrast, the IX PL barely changes between $n = -1$ and 1 in the R-stacked device.

We now examine the electron–IX interaction on the basis of these understandings. At $n = 1$, the lower Hubbard band (LHB) of C1 is fully occupied with electrostatically doped electrons. Therefore, the IX consists of an electron in the upper Hubbard band (UHB) of C1 and a hole in the flat band V1, as illustrated in Fig. 2e. The electrons in the LHB of C1 will interact with the electron–hole pair of the IX and contribute both a repulsion term, U_{e-e}, and an attraction term, V_{e-h}. The total electron–IX repulsion energy is thus $U_{e-IX}(n = 1) \approx U_{e-e} - V_{e-h}$, which corresponds to the energy blueshift observed in our experiment. The scenario at $n = -1$ is similar (Fig. 2f), except that the repulsion is between IX hole and the holes in the UHB of V1 with a repulsion term U_{h-h} and an attraction term V_{e-h}; then we can write $U_{e-IX}(n = -1) \approx U_{h-h} - V_{e-h}$.

The first major experimental observation can be understood with the extended IX in the H-stacking, which suggests a smaller V_{e-h}. As a result, we expect the blueshift to be larger in H-stacked devices, which explains our first major observation in Fig. 1e,f that the blueshifts in H-stacked device are larger at $n = \pm1$. Second, we have estimated the onsite repulsion energies (U_{e-e} and U_{h-h}) for different valence and conduction bands using the localization of the wavefunctions (details in Supplementary Section 9). The electron–electron repulsion (U_{e-e}) is larger than hole–hole repulsion (U_{h-h}) in the same stack configuration, which well explains our second major observation of the larger blueshift observed for $n = 1$ than for $n = -1$ in Fig. 1e,f.

In Fig. 1e,f, we also observe that the blueshift is about 0 meV at both $n = \pm2$ for the R-stacked device, whereas the blueshift is around 17 meV and around 15 meV for the H-stacked device at $n = +2$ and −2, respectively. We notice that the blueshift is generally smaller at $n = \pm2$ compared with that at $n = \pm1$ for both R-stacked and H-stacked devices, which coincide with previous observations that the $n = \pm1$ states have a higher transition temperature than $n = \pm2$, hence a larger energy gap at $n = \pm1$ (refs. 2–4). We also observe an additional PL peak around 1.39 eV on the hole side in R-stacked devices, potentially owing to the attractive

https://doi.org/10.1038/s41567-023-02266-2

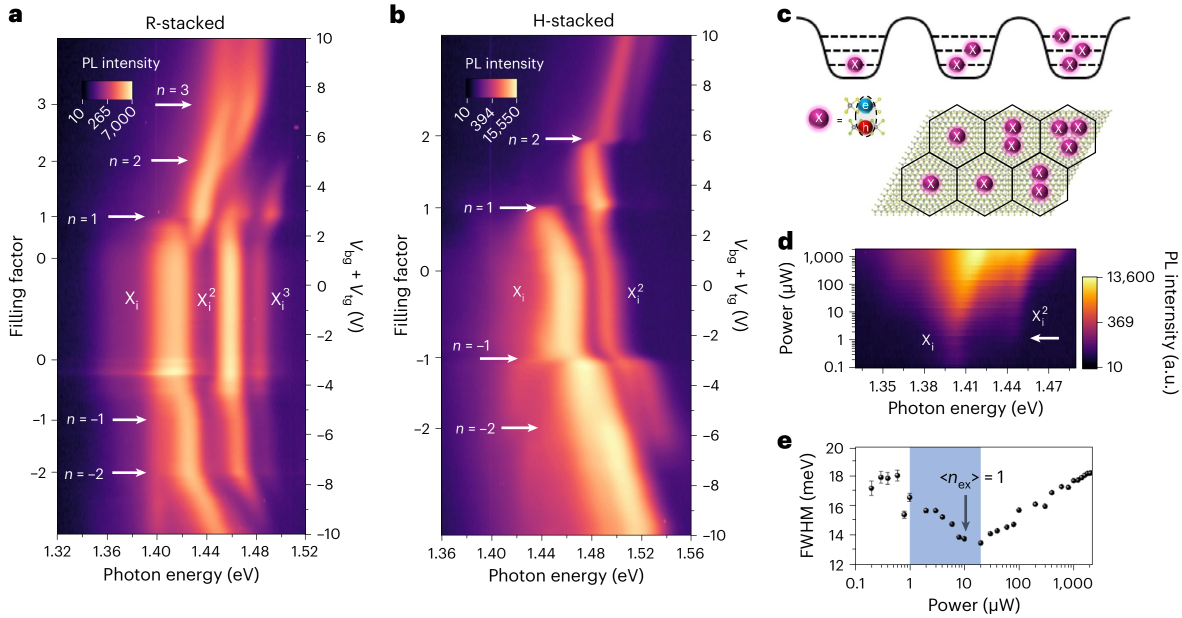

Fig. 3 | Excitonic Mott state formation with increased exciton density. **a**,**b**, Doping-dependent PL spectra with an increased optical excitation power of 300 μW (corresponds to an average exciton density around 1.7×10^{13} cm^{-2}), with the CW excitation photon energy centred at 1.96 eV. **c**, A schematic of the excitonic Mott insulator with some moiré unit cells having double or triple exciton occupancy. **d**, Excitation power dependence of the PL spectra of R-stacked device R1, with a CW excitation photon energy centred at 1.70 eV. a.u., arbitrary unit. **e**, The full-width at half-maximum (FWHM) of the fitted Lorentzian peaks extracted from **d**, plotted as a function of the optical excitation power. The error bars indicate the standard errors extracted from the fitting. The blue-shaded region highlights the FWHM decreases with the increasing excitation power. All the data were taken at a temperature of 4.2–5.0 K. $<n_{ex}>$ indicates the estimated average exciton density.

interlayer trion with a binding energy of about 8 meV, which is not the focus of the current work and will be explored later.

Understanding the blueshift at the $n = \pm 2$ states is more complicated, as it involves the nature of the insulating states, the bandgaps (Δ_e and Δ_h) and the repulsion energy involving C2 and V2. In Supplementary Section 10, we provide a simple model to attempt to explain the observations, yet a complete understanding requires future work to refine the model and calculations. We emphasize here that our experimental observations of $n = \pm 2$ states, shown in Fig. 1e,f, are reproduced in over six R-stacked and six H-stacked devices, providing valuable guidance for further theoretical understandings.

The strong Coulomb interaction in the WS_2/WSe_2 moiré superlattice enhances not only the electron–IX interaction but also the IX–IX interaction, making it possible to realize the bosonic Mott state composed of IXs. Indeed, as we increase the optical excitation power, new PL peaks emerge at higher energies, labelled as X_i^2 and X_i^3 in Fig. 3a,b. The PL peak X_i^2 has an onset excitation power of 1–25 μW in most devices, and we have reproduced X_i^2 in six R-stacked devices and six H-stacked devices. The detailed excitation power dependence of the doping-dependent PL spectra of six typical devices is shown in Extended Data Fig. 3. The PL peak X_i^3 occurs at a much higher excitation power, typically hundreds of microwatts (Fig. 3a). We have only observed it in four R-stacked devices, not in any of the H-stacked devices. We rule out the possibility of these new PL peaks being the excited states of IX from other moiré sites or conduction bands, as those should exhibit an opposite valley polarization to the ground state IX, which contradicts our observations in Fig. 4 (ref. 23). Furthermore, the fact that the higher energy PL peaks are absent for $n > 1$ in the H-stacking also rules out those possibilities.

We attribute X_i^2 to the blueshifted IX PL in the presence of a bosonic Mott insulator of IXs[24] (Fig. 3c), which emerges when each moiré unit cell is filled with one IX. Any additional IX will then create a double occupancy in one moiré unit cell. Hence, the IX–IX repulsion increases the IX energy. This state is simply a bosonic analogue of an electron Mott insulator. To examine this picture, we measure the power dependence of the PL spectra in the R-stacked device R1 (Fig. 3d). The extracted linewidth of X_i decreases when the excitation power increases from 1 μW to 20 μW (blue-shaded area in Fig. 3e). This behaviour is surprising because an increased IX–IX interaction at higher IX densities is expected in general to shorten the IX lifetime, which would broaden the linewidth. By contrast, it can be well explained if we consider the formation of a bosonic Mott insulator of IXs, in which IXs are localized. The excitation power at which the linewidth starts to decrease also coincides with the onset of the X_i^2 as marked by the white arrow in Fig. 3d. Furthermore, we estimate the order of magnitude of excitation power needed to generate an IX density of one IX per moiré unit cell to be about 10 μW (Supplementary Section 5), which is consistent with the typical onset excitation power in the range of 1–25 μW observed in six R-stacked devices and five H-stacked devices. A more detailed analysis of the excitation power dependence can be found in Supplementary Section 5.

The IX–IX repulsion energy (U_{ex-ex}), which we estimate from the energy difference between X_i^2 and X_i, is about 44 meV for the R-stacked device R1 and about 32 meV for the H-stacked device H1. The reduced IX–IX repulsion is consistent with the extended nature of the IX wavefunction in the H-stacking, which suggests a shallower energy trap for IX[25]. For the same reason, the H-stacked device cannot host three excitons in one moiré unit cell, but the R-stacked device can (X_i^3), albeit with a reduced IX–IX repulsion, about 20 meV estimated from the difference between X_i^3 and X_i^2. The apparent asymmetry of X_i^2 (and X_i^3 in R-stacking) as a function of the doping remains an intriguing subject to be explored in the future. It is worth noting here that the observed U_{ex-ex} is more than one order of magnitude larger than that in the double quantum wells made of GaAs/AlGaAs[26,27], thus enabling an excitonic Mott state at a much higher temperature[28].

Finally, we have performed helicity-resolved PL spectroscopy measurements in both R-stacked and H-stacked devices (R1 and H1) using continuous wave (CW) laser excitation centred at 1.70 eV,

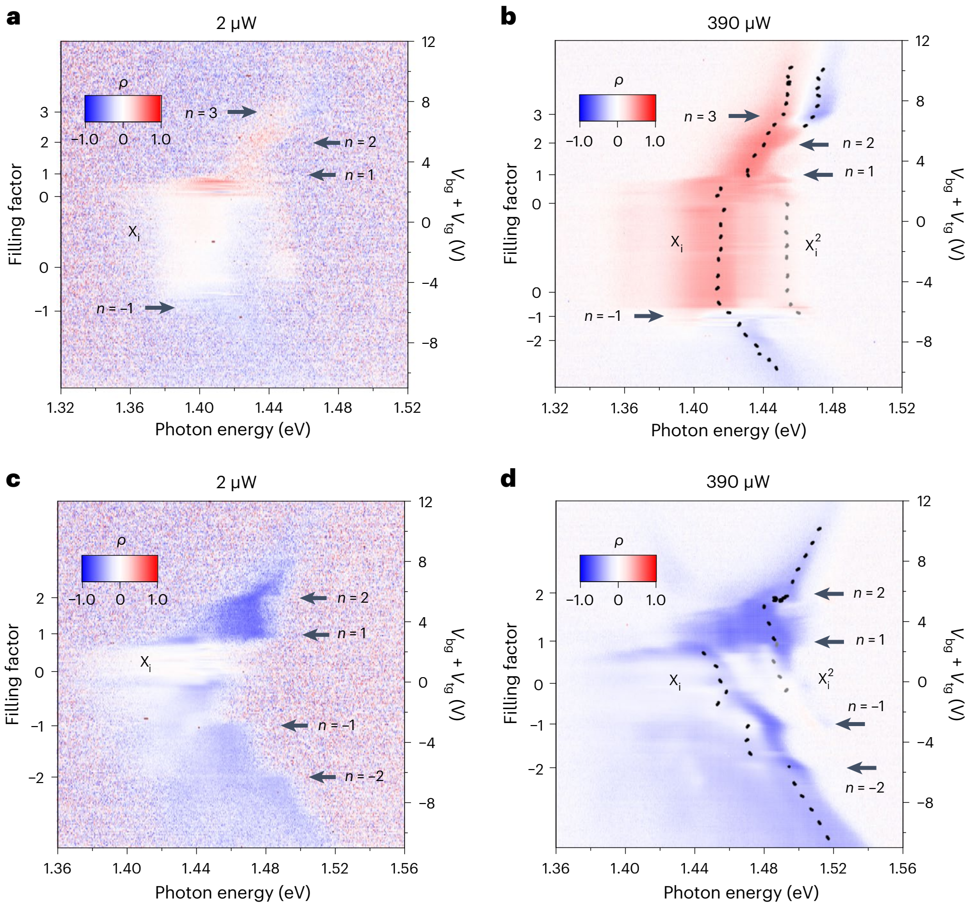

Fig. 4 | Valley polarization of the excitonic Mott insulator. a,**b**, Doping-dependent circular polarization of PL of the R-stacked device R1 under an excitation power of 2 μW (average exciton density around 3.5×10^{11} cm^{-2}) (**a**) and 390 μW (average exciton density around 6.9×10^{13} cm^{-2}) (**b**). **c**,**d**, Doping-dependent circular polarization of PL of the H-stacked device H1 under an excitation power of 2 μW (**c**) and 390 μW (**d**). A CW laser with photon energy centred at 1.70 eV was used for the optical excitation, and all data were taken at a temperature of 5.0 K.

resonantly exciting the moiré A exciton of WSe_2 (details in Methods). The extracted PL circular polarization, ρ, is plotted as a function of doping, as shown in Fig. 4. Under a low excitation power of 2 μW (Fig. 4a), for the R-stacked device R1, the PL is co-circularly polarized with respect to the excitation in both charge-neutral and electron-doped regions, whereas the PL is cross-polarized in the highly p-doped region. However, for the H-stacked device H1 (Fig. 4c), ρ is close to zero near the charge-neutral region but cross-polarized in both highly n-doped and p-doped regions. The circular polarization of the R-stacked and H-stacked WS_2/WSe_2 moiré superlattice can be well understood by considering the optical selection[29,30], the long valley lifetime of holes and the efficient intervalley scattering of electrons[31], owing to the vastly different spin–orbit coupling magnitude in the conduction and valence bands. Detailed explanations can be found in Supplementary Section 11.

Here we note that above $n = 2$, the circular polarization of the emerging IX PL branch near 1.46 eV in the R-stacked sample reverses sign, suggesting that the added IX will have its electron occupying the second conduction band (the LHB of C2 to be precise, with an opposite spin as opposed to C1) (detailed discussion in Supplementary Section 11).

As we increase the excitation power, there are two major changes to the circular polarization spectra in the charge-neutral region of device R1 (Fig. 4a,b). First, ρ of the IX ground state (X_i) increases by a large amount. Second, the second PL peak (X_i^2) also exhibits a finite valley polarization that has the same sign as X_i. The latter rules out the possibility of X_i^2 being excitons from another moiré site or conduction band, as those will switch the sign of ρ. The enhanced circular polarization is striking, which increases from 7% (Fig. 4a) to 50% (Fig. 4b) in the charge-neutral region $n = 0$, an increase by nearly one order of magnitude. The presence of X_i^2 indicates the formation of the bosonic Mott insulator state. The enhancement of PL valley polarization of X_i, therefore, is strongly tied to the strong exciton correlation. The strongly enhanced valley polarization could possibly arise from the suppressed valley scattering of IXs at the bosonic Mott insulator state or even optical-pumping-induced ferromagnetism[32,33], although its exact nature needs to be further explored. The valley-polarized excitons usher new venues for exploring correlated excitons that do not exist in other systems and inspire future exploration of valley physics in strongly correlated bosonic systems.

Online content

Any methods, additional references, Nature Portfolio reporting summaries, source data, extended data, supplementary information, acknowledgements, peer review information; details of author contributions and competing interests; and statements of data and code availability are available at https://doi.org/10.1038/s41567-023-02266-2.

References

1. Regan, E. C. et al. Mott and generalized Wigner crystal states in WSe_2/WS_2 moiré superlattices. *Nature* **579**, 359–363 (2020).
2. Tang, Y. et al. Simulation of Hubbard model physics in WSe_2/WS_2 moiré superlattices. *Nature* **579**, 353–358 (2020).
3. Huang, X. et al. Correlated insulating states at fractional fillings of the WS_2/WSe_2 moiré lattice. *Nat. Phys.* **17**, 715–719 (2021).

4. Xu, Y. et al. Correlated insulating states at fractional fillings of moiré superlattices. *Nature* **587**, 214–218 (2020).
5. Jin, C. et al. Stripe phases in WSe_2/WS_2 moiré superlattices. *Nat. Mater.* **20**, 940–944 (2021).
6. Li, T. et al. Quantum anomalous Hall effect from intertwined moiré bands. *Nature* **600**, 641–646 (2021).
7. Li, T. et al. Continuous Mott transition in semiconductor moiré superlattices. *Nature* **597**, 350–354 (2021).
8. Stansbury, C. H. et al. Visualizing electron localization of WS_2/WSe_2 moiré superlattices in momentum space. *Sci. Adv.* **7**, eabf4387 (2021).
9. Hubbard, J. Electron correlations in narrow energy bands. *Proc. R. Soc. Lond. Ser. A* **276**, 238–257 (1963).
10. Wu, F., Lovorn, T., Tutuc, E. & Macdonald, A. H. Hubbard model physics in transition metal dichalcogenide moiré bands. *Phys. Rev. Lett.* **121**, 26402 (2018).
11. Wang, G. et al. Colloquium: excitons in atomically thin transition metal dichalcogenides. *Rev. Mod. Phys.* **90**, 21001 (2018).
12. Xu, X., Yao, W., Xiao, D. & Heinz, T. F. Spin and pseudospins in layered transition metal dichalcogenides. *Nat. Phys.* **10**, 343–350 (2014).
13. Mak, K. F. & Shan, J. Photonics and optoelectronics of 2D semiconductor transition metal dichalcogenides. *Nat. Photon.* **10**, 216–226 (2016).
14. Bloch, I., Dalibard, J. & Zwerger, W. Many-body physics with ultracold gases. *Rev. Mod. Phys.* **80**, 885–964 (2008).
15. Gemelke, N., Zhang, X., Hung, C. L. & Chin, C. In situ observation of incompressible Mott-insulating domains in ultracold atomic gases. *Nature* **460**, 995–998 (2009).
16. Rivera, P. et al. Interlayer valley excitons in heterobilayers of transition metal dichalcogenides. *Nat. Nanotechnol.* **13**, 1004–1015 (2018).
17. Jin, C. et al. Ultrafast dynamics in van der Waals heterostructures. *Nat. Nanotechnol.* **13**, 994–1003 (2018).
18. Gersch, H. A. & Knollman, G. C. Quantum cell model for bosons. *Phys. Rev.* **129**, 959–967 (1963).
19. Miao, S. et al. Strong interaction between interlayer excitons and correlated electrons in WSe_2/WS_2 moiré superlattice. *Nat. Commun.* **12**, 3608 (2021).
20. Chen, D. et al. Tuning moiré excitons and correlated electronic states through layer degree of freedom. *Nat. Commun.* **13**, 4810 (2022).
21. Chen, D. et al. Excitonic insulator in a heterojunction moiré superlattice. *Nat. Phys.* **18**, 1171–1176 (2022).
22. Wang, X. et al. Intercell moiré exciton complexes in electron lattices. *Nat. Mater.* **22**, 599–604 (2023).
23. Jin, C. et al. Identification of spin, valley and moiré quasi-angular momentum of interlayer excitons. *Nat. Phys.* **15**, 1140–1144 (2019).
24. Xiong, R. et al. Correlated insulator of excitons in WSe_2/WS_2 moiré superlattices. *Science* **380**, 860–864 (2023).
25. Yuan, L. et al. Twist-angle-dependent interlayer exciton diffusion in WS_2–WSe_2 heterobilayers. *Nat. Mater.* **19**, 617–623 (2020).
26. Lagoin, C., Suffit, S., Baldwin, K., Pfeiffer, L. & Dubin, F. Mott insulator of strongly interacting two-dimensional semiconductor excitons. *Nat. Phys.* **18**, 149–153 (2022).
27. Lagoin, C. et al. Extended Bose–Hubbard model with dipolar excitons. *Nature* **609**, 485–489 (2022).
28. Sugawa, S. et al. Interaction and filling-induced quantum phases of dual Mott insulators of bosons and fermions. *Nat. Phys.* **7**, 642–648 (2011).
29. Yu, H., Liu, G. B., Tang, J., Xu, X. & Yao, W. Moiré excitons: from programmable quantum emitter arrays to spin–orbit-coupled artificial lattices. *Sci. Adv.* **3**, e1701696 (2017).
30. Yu, H., Liu, G.-B. & Yao, W. Brightened spin-triplet interlayer excitons and optical selection rules in van der Waals heterobilayers. *2D Mater.* **5**, 35021 (2018).
31. Kim, J. et al. Observation of ultralong valley lifetime in WSe_2/MoS_2 heterostructures. *Sci. Adv.* **3**, e1700518 (2017).
32. Wang, X. et al. Light-induced ferromagnetism in moiré superlattices. *Nature* **604**, 468–473 (2022).
33. Hao, K., Shreiner, R., Kindseth, A. & High, A. A. Optically controllable magnetism in atomically thin semiconductors. *Sci. Adv.* **8**, eabq7650 (2022).

https://doi.org/10.1038/s41567-023-02266-2

Methods

Device fabrication

We used a dry pick-up method, as reported in our earlier work[21] to fabricate angle-aligned WS_2/WSe_2 heterobilayers. For the device shown in the main text, during the pick-up process, we tear one WS_2 monolayer into two pieces, rotate one piece by 180° and align both pieces with one single WSe_2 monolayer to get both R-stacked and H-stacked devices on one chip. The fabricated devices were then annealed at 250 °C in a vacuum for 500 min.

Optical characterizations

The optical measurements were performed under a home-built confocal microscope, with the sample cooled by either a liquid helium-flow-controlled optical cryostat (Janis) or a cryogen-free optical cryostat (Montana Instruments). The excitation laser was focused on the sample with a beam spot diameter of about 2 µm, and the optical signals were collected by a spectrometer (Princeton Instruments). The PL measurements in Figs. 1 and 3a,b and Extended Data Figs. 1 and 3 were performed with a CW laser centred at 1.96 eV. All other PL measurements were performed with a CW laser centred at 1.70 eV. To perform helicity-resolved measurements, a quarter waveplate was placed before the objective to convert the excitation laser to σ^+ polarized light and circularly polarized PL emission to linearly polarized light. The σ^+ and σ^- PL emission was analysed using a half waveplate and a polarizer. The doping-dependent PL spectra in the right (σ^+) and left σ^-) circularly polarized channels can be found in Extended Data Figs. 4–6. The extracted PL circular polarization is expressed as $\rho = \frac{I^+ - I^-}{I^+ + I^-}$, in which I^+ and I^- denote the intensities of σ^+ and σ^- PL emission. The reflectance contrast measurements were performed with a super-continuum laser (YSL Photonics). The polarized second-harmonic generation (SHG) measurements were performed with a pulsed laser excitation centred at 800 nm (Ti:sapphire; Coherent Chameleon) with a repetition rate of 80 MHz and a power of 100 mW. The crystal axes of the sample were fixed. A half waveplate is placed between the beam splitter and the objective to change the polarization angle of both the excitation laser and the SHG signal. The SHG signal was analysed using a polarizer. The details of time-resolved PL measurements and exciton density estimate can be found in Supplementary Sections 4 and 5, respectively.

Electronic structure calculations

The twisted WS_2/WSe_2 heterobilayer structures are generated using the TWISTER package[34]. Structural relaxations are performed using the LAMMPS (Large-scale Atomic/Molecular Massively Parallel Simulator) package[35,36]. The electronic structure calculations are performed using the SIESTA (Spanish Initiative for Electronic Simulations with Thousands of Atoms) package[37] based on the density functional theory[38]. See Supplementary Section 7 for details.

Data availability

Source data are provided with this paper. All other data that support the plots within this paper and other findings of this study are available from the corresponding authors upon reasonable request.

Code availability

The twisted bilayer structure construction, atomic relaxations and electronic band structure calculations presented in this paper were carried out using publicly available codes. Our findings can be fully reproduced by the use of these codes and by following the procedure outlined in the paper.

References

34. Naik, S., Naik, M. H., Maity, I. & Jain, M. Twister: construction and structural relaxation of commensurate moiré superlattices. *Comput. Phys. Commun.* **271**, 108184 (2022).
35. Thompson, A. P. et al. LAMMPS—a flexible simulation tool for particle-based materials modeling at the atomic, meso, and continuum scales. *Comput. Phys. Commun.* **271**, 108171 (2022).
36. Plimpton, S. et al. LAMMPS molecular dynamics simulator. *Sandia National Laboratories* https://lammps.org/ (2023).
37. Soler, J. M. et al. The SIESTA method for ab initio order-*N* materials simulation. *J. Phys. Condens. Matter* **14**, 2745–2779 (2002).
38. Perdew, J. P. & Zunger, A. Self-interaction correction to density-functional approximations for many-electron systems. *Phys. Rev. B* **23**, 5048–5079 (1981).

Acknowledgements

We thank C. Jin for the helpful discussions. Z.L. and S.-F.S. acknowledge support from NYSTAR through Focus Center-NY-RPI Contract C150117. The device fabrication was supported by the Micro and Nanofabrication Clean Room at Rensselaer Polytechnic Institute (RPI). S.-F.S. also acknowledges the support from NSF (Career Grant DMR-1945420, DMR-2104902 and ECCS-2139692). X.H., Q.W. and Y.-T.C. acknowledge support from NSF under awards DMR-2104805 and DMR-2145735. The optical spectroscopy measurements were supported by the Air Force Office of Scientific Research (AFOSR) under DURIP awards through Grants FA9550-20-1-0179 and FA9550-23-1-0084. I.M. acknowledges funding from the European Union's Horizon 2020 Research and Innovation programme under the Marie Skłodowska-Curie Grant agreement no. 101028468. This work used the ARCHER2 UK National Supercomputing Service (https://www.archer2.ac.uk). S.T. acknowledges support from DOE-SC0020653, Applied Materials Inc., NSF CMMI 1825594, NSF DMR-1955889, NSF CMMI-1933214, NSF DMR-1904716, NSF 1935994 and NSF ECCS 2052527 and DMR 2111812. K.W. and T.T. acknowledge support from the Elemental Strategy Initiative conducted by the MEXT, Japan, Grant Numbers JPMXP0112101001 and JSPS KAKENHI, Grant Numbers 19H05790 and JP20H00354.

Author contributions

S.-F.S. conceived the project. Y.M., Z.L. and D.C. fabricated heterostructure devices. Z.L., L.M., L.Y. and Y.M. performed the optical spectroscopy measurements. M.B. and S.T. grew the TMDC crystals. T.T. and K.W. grew the BN crystals. I.M. and J.L. performed the DFT calculations. S.-F.S., Y.-T.C., Z.L., Y.M., Xiaotong Chen and Xinyue Chen analysed the data. S.-F.S. and Y.-T.C. wrote the paper with input from all authors.

Competing interests

The authors declare no competing interests.

Additional information

Extended data is available for this paper at https://doi.org/10.1038/s41567-023-02266-2.

Supplementary information The online version contains supplementary material available at https://doi.org/10.1038/s41567-023-02266-2.

Correspondence and requests for materials should be addressed to Yong-Tao Cui or Su-Fei Shi.

Peer review information *Nature Physics* thanks Nadine Leisgang, Fengcheng Wu and the other, anonymous, reviewer(s) for their contribution to the peer review of this work.

https://doi.org/10.1038/s41567-023-02266-2

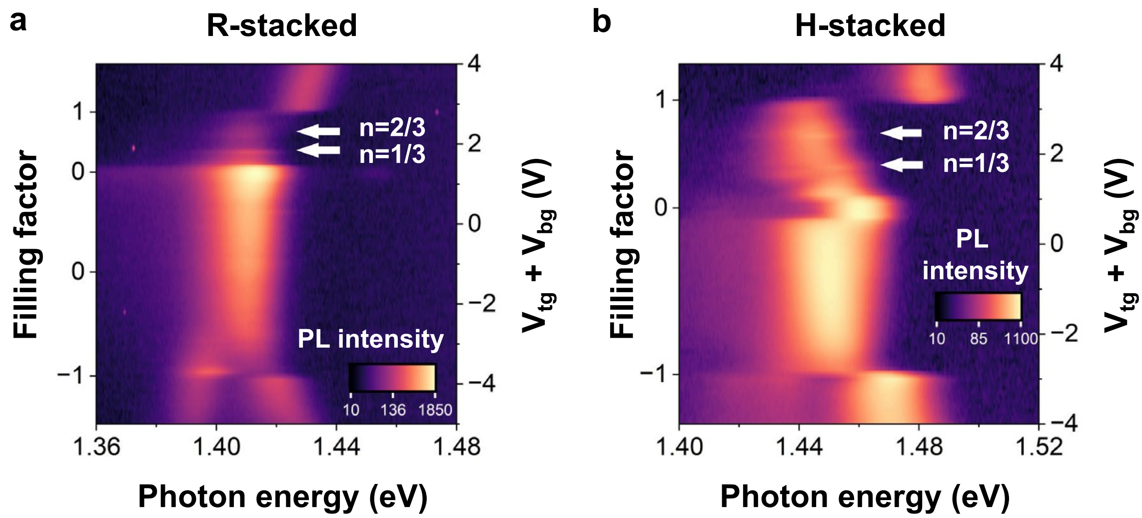

Extended Data Fig. 1 | Zoom-ins of the doping-dependent PL spectra. (**a**) and (**b**) are the Zoom-ins of doping-dependent PL spectra in Fig. 1c,d, respectively.

https://doi.org/10.1038/s41567-023-02266-2

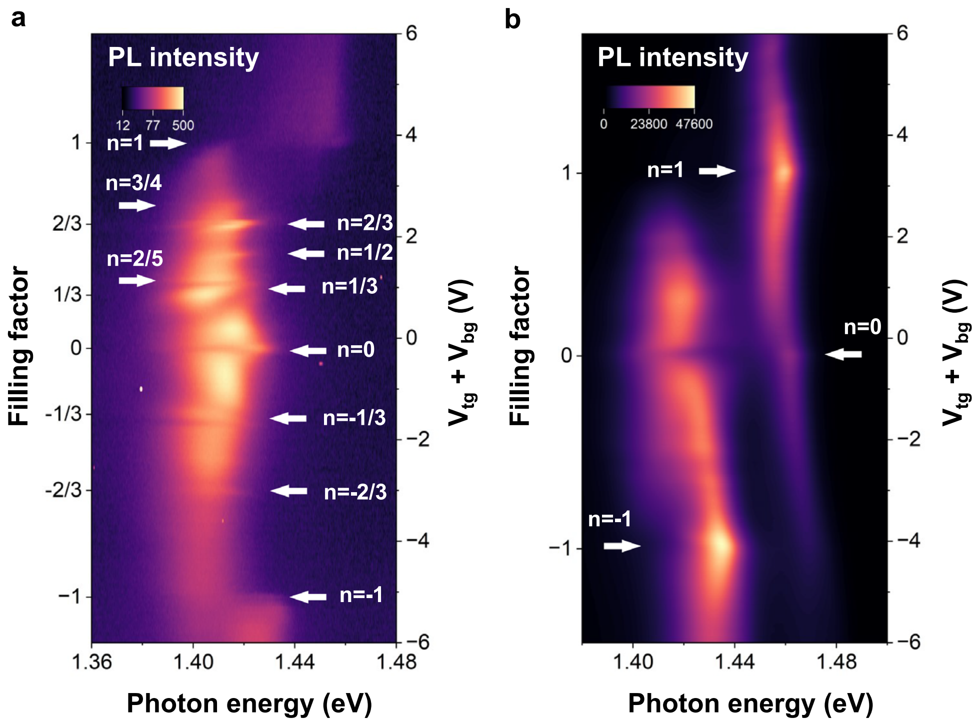

Extended Data Fig. 2 | PL spectra of an H-stacked device showing more fractional fillings. (**a**) and (**b**) are the doping-dependent PL spectra measured on device H5 using an excitation power of 0.2 μW and 300 μW, respectively. A CW laser with photon energy centered at 1.70 eV was used for the optical excitation, and all data were taken at a temperature of 5.0 K.

 https://doi.org/10.1038/s41567-023-02266-2

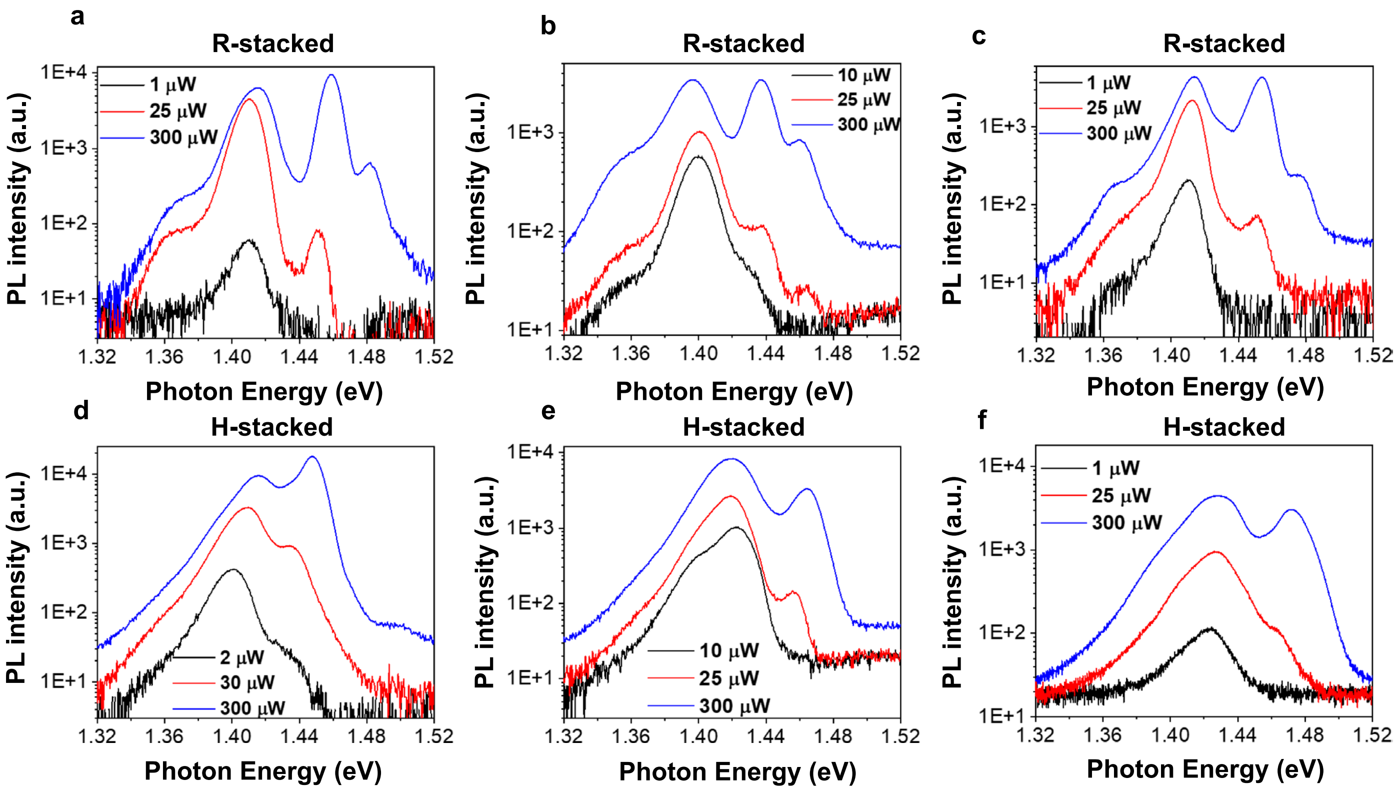

Extended Data Fig. 3 | Power-dependent PL spectra for different R-stacked and H-stacked devices around n = 0. (**a**), (**b**) and (**c**) are the power-dependent PL spectra of R-stacked devices R1, R2 and R3, respectively. (**d**), (**e**) and (**f**) are the power-dependent PL spectra of H-stacked devices H2, H3 and H4, respectively. Black, red, and blue line show PL spectra under low, medium, and high excitation power. A CW laser with photon energy centered at 1.96 eV was used for the optical excitation, and all data were taken at a temperature of 4–10 K.

https://doi.org/10.1038/s41567-023-02266-2

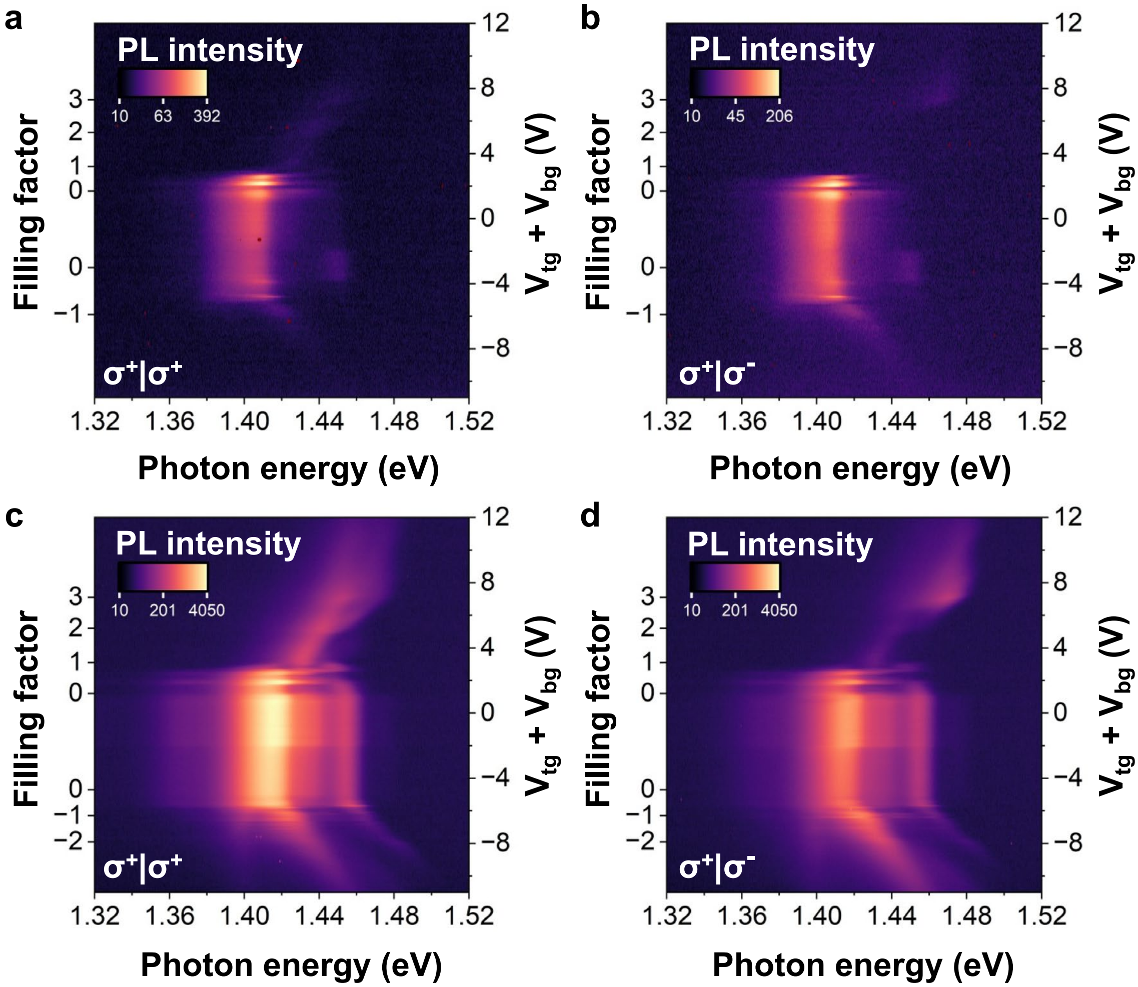

Extended Data Fig. 4 | Helicity-resolved doping-dependent PL spectra for R-stacked WS_2/WSe_2 moiré bilayers under different excitation powers. (**a**) and (**b**) are the measured right (σ^+) and left circularly (σ^-) polarized doping-dependent PL spectra of device R1, under a σ^+ excitation with the excitation power of 2 µW. (**c**) and (**d**) are σ^+ and σ^- PL spectra under a σ^+ excitation with an excitation power of 390 µW. A CW laser with photon energy centered at 1.70 eV was used for the optical excitation, and all data were taken at a temperature of 5.0 K.

 https://doi.org/10.1038/s41567-023-02266-2

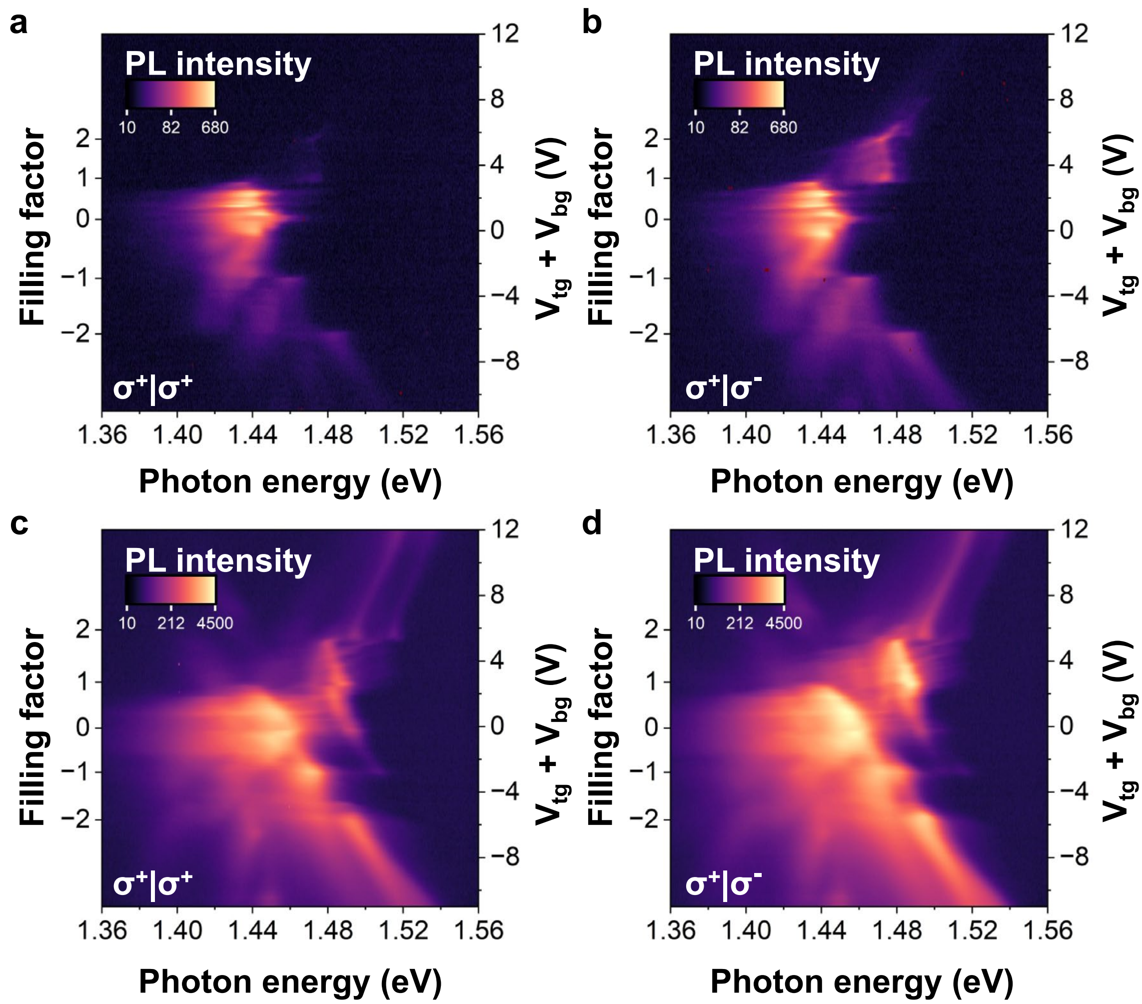

Extended Data Fig. 5 | Helicity-resolved doping-dependent PL spectra for H-stacked moiré bilayers under different power. (**a**) and (**b**) are the measured right (σ^+) and left circularly (σ^-) polarized doping-dependent PL spectra of device H1, under a σ^+ excitation with an excitation power of 2 μW. (**c**) and (**d**) are σ^+ and σ^- PL spectra under a σ^+ excitation with an excitation power of 390 μW. A CW laser with photon energy centered at 1.70 eV was used for the optical excitation, and all data were taken at a temperature of 5.0 K.

https://doi.org/10.1038/s41567-023-02266-2

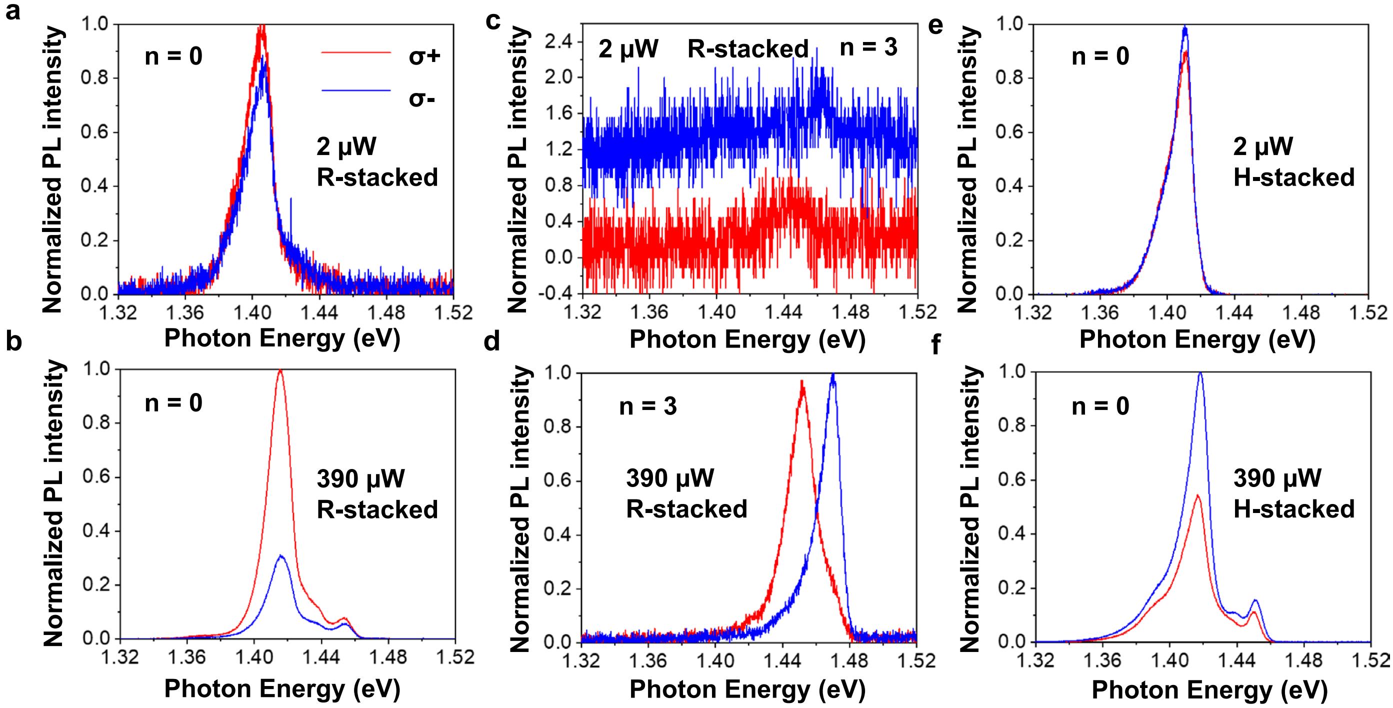

Extended Data Fig. 6 | Helicity-resolved PL spectra of device R1 and H1 for various filling factors and under different excitation powers. (**a**) and (**b**) are the PL spectra of device R1 at n = 0 under excitation powers of 2 μW and 390 μW, respectively. The red and blue lines represent measured right (σ^+) and left circularly (σ^-) polarized PL spectra, respectively, under the σ^+ excitation. (**c**) and (**d**) are the PL spectra of device R1 at n = 3 under the excitation power of 2 μW and 390 μW, respectively. (**e**) and (**f**) are the PL spectra of device H1 at n = 0 with excitation power of 2 μW and 390 μW, respectively. These data are extracted from Extended Data Figs. 4 and 5. The data in (**c**) are offset for the clarity of presentation.